The Cryosphere Discuss., 4, 901–947, 2010
www.the-cryosphere-discuss.net/4/901/2010/
doi:10.5194/tcd-4-901-2010

The Cryosphere Discussions

Permafrost and surface energy balance of a polygonal tundra site in northern Siberia – Part 1: Spring to fall

M. Langer, S. Westermann, S. Muster, K. Piel, and J. Boike

Alfred-Wegener-Institute for Polar and Marine Research, Telegrafenberg A43, 14473 Potsdam, Germany

Received: 17 June 2010 – Accepted: 23 June 2010 – Published: 12 July 2010

Correspondence to: M. Langer (moritz.langer@awi.de)

Published by Copernicus Publications on behalf of the European Geosciences Union.

Abstract

Permafrost thawing is essentially determined by the surface energy balance, which potentially triggers the activation of a massive carbon source, if previously frozen organic soils are exposed to microbial decomposition. In this article, we present the first part of a comprehensive annual surface energy balance study performed at a polygonal tundra landscape in northeast Siberia, realized between spring 2007 and winter 2009. This part of the study focuses on the half year period from April to September 2007–2008, during which the surface energy balance is obtained from independent measurements of the radiation budget, the turbulent heat fluxes and the ground heat flux at several sites. The short-wave radiation is the dominant factor in the surface energy balance during the entire observation period. About 50% of the available net radiation is consumed by latent heat flux, while the sensible and the ground heat flux are both on the order of 20 to 30%. The ground heat flux is mainly consumed by active layer thawing, where 60% of soil energy storage are attributed to. The remainder is used for soil warming down to a depth of 15 m. The controlling factors for the surface energy partitioning are in particular the snow cover, the cloud cover and the soil temperature gradient. Significant surface temperature differences of the heterogeneous landscape indicate spatial variabilities of sensible and latent heat fluxes, which are verified by measurements at different locations. However, differences in the partition between sensible and latent heat flux for the different sites only exist during conditions of high radiative forcing, which only occur occasionally.

1 Introduction

The thermal state of permafrost and its susceptibility towards degradation is fundamentally determined by the surface energy balance. Recent studies revealed that essential climate changes take place in the Arctic and are expected to proceed in the future (Overpeck et al., 1997; Hansen et al., 2001; Comiso, 2006; Overland et al., 2008).

TCD
4, 901–947, 2010

There is observational evidence that energy and water exchange processes in the arctic landscapes are already substantially affected, which also involves the thermal state of permafrost (Serreze et al., 2000; Hinzman et al., 2005). Permafrost, which occupies about 25% of the land area of the Northern Hemisphere (Brown et al., 1997), is considered an important factor in the complex feedback mechanisms of the climate system due to its massive carbon storage capabilities (Christensen and Cox, 1995; Callaghan et al., 2004; McGuire et al., 2006). Zimov et al. (2006) estimated that about 970 Gt of carbon are stored in permafrost soils worldwide, which is about twice the amount of the actual atmospheric carbon concentration. Until now it is unclear whether permafrost regions will turn into massive sources of greenhouse gases, such as methane and carbon dioxide, as the frozen soils begin to thaw (Hobbie et al., 2000; Davidson and Janssens, 2006). This raises the question about the amount of stored organic material that will be exposed to microbial decomposition according to permafrost degradation and progressing thaw depths under a warming climate. Recent measurements at wet tundra landscapes demonstrate the importance of the freeze and thaw dynamics for methane emission, which are related in a non-linear manner (Christensen et al., 2003; Sachs et al., 2008; Mastepanov et al., 2008). For this purpose, efforts have been initiated to incorporate permafrost and the annual freeze and thaw dynamics in global climate models (e.g. Stendel and Christensen, 2002; Lawrence and Slater, 2005; Nicolsky et al., 2007; Lawrence et al., 2008). However, the energy exchange processes at the soil-atmosphere interface strongly depend on the landscape characteristics, such as surface moisture, vegetation cover, snow cover and soil properties. These characteristics are incorporated in climate models as parameterizations of e.g. surface roughness, resistance to evaporation and thermal properties of soil or snow. The representation of permafrost in climate models therefore essentially depends on the parameterization that is used to describe the surface energy balance. To support and validate modeling, it is desirable to obtain process studies, which deliver important information about the landscape specific energy balance characteristics and their determining factors. Long-term energy balance studies are especially important in arctic regions, where the

TCD
4, 901–947, 2010

surface energy budget is characterized by an extreme seasonality and meteorological measurements are sparse (Westermann et al., 2009).

This study presents the annual energy balance of a wet tundra landscape in northern Siberia from spring 2007 until winter 2009. The study has been performed at a site dominated by polygonal tundra, which is a typical arctic landscape. Based on standard meteorological measurements Boike et al. (2008) contrasts the energy and water balances of a wet and a dry summer at the study site. In this study, we extend this previous work over the entire annual cycle by using independent measurements of all components of the surface energy balance. Furthermore, we investigate the impact of the considerable surface heterogeneity of the wet tundra landscape on the regional energy balance. The results of this study are presented in two parts: Part I comprises the period from April to September, which is characterized by increasing soil temperatures at the study site. Part II focuses on the winter period from October to March, which represents the period of soil cooling (Langer et al., 2010b).

The aim of the study is (i) to evaluate the annual surface energy balance at the study site, (ii) to determine the controlling and limiting factors in the energy partitioning and the transport processes, (iii) to evaluate the seasonal and inter-annual variability and (iv) to elucidate the impact of surface heterogeneities on the energy balance at the landscape scale.

2 Study site

The study site is located on Samoylov Island (72°22′ N; 126°30′ E) at the upper part of the Lena River Delta (Fig. 1). It is characterized by a wet tundra landscape typical of northern Siberia. Samoylov Island covers an area of about 4.5 km^2 with an elevated eastern terrace and a lower western flood plain. The region features a typical arctic-continental climate with a mean annual air temperature (MAAT) of about −13 °C and a total annual precipitation around 250 mm (Boike et al., 2008). The ice break-up of the Lena River and the snow melt usually start at beginning of June. The snow-free period

TCD
4, 901–947, 2010

lasts until the end of September, during which maximum air temperatures of about 20 °C are reached. The regional climate and the synoptic conditions are influenced by both the Siberian High and the Polar Low pressure system. During the summer period, intermediate cyclone activity with low intensity are typically observed, while cyclones with high intensity, but short lifetime are more frequently found in winter (Zhang et al., 2004). However, the strong Siberian High strongly affects the Lena Delta region during the winter months and causes air temperatures to fall frequently below −45 °C. The study site is in the zone of continuous permafrost, with permafrost depths reaching 500 to 600 m in the wider area around the study site (Grigoriev, 1960). The soil temperatures are very low: in the depth of the zero annual amplitude (approximately 15 m), the soil temperatures are about −10 °C. The maximum thaw depths during summer range from 0.40 to 0.50 m. The permafrost landscape features characteristic polygonal surface structures, which are typical for the wet tundra landscapes. These patterns are 50 to 100 m^2 large and usually consist of dry elevated rims and depressed centers, which are filled with water-saturated peat soils or shallow ponds. The vegetation at the wet centers is dominated by hydrophilic sedges and mosses, while the elevated dry rims are dominated by mesophytic dwarf shrubs, forbs and mosses. For a more detailed description of the vegetation and landscape characteristics, refer to Are and Reimnitz (2000), Kutzbach et al. (2004), Kutzbach et al. (2007), Boike et al. (2008) and Sachs et al. (2008).

3 Methods

The energy balance equation is written as

$$Q_{net} = Q_H + Q_E + Q_G + [Q_{melt}] + C, \quad (1)$$

where Q_{net} denotes the net radiation, Q_H the atmospheric sensible heat flux, Q_E the atmospheric latent heat flux, Q_G the ground heat flux, Q_{melt} is the energy flux consumed by the snow melt, which can be inferred from to the energy required to thaw the snow

TCD
4, 901–947, 2010

pack, E_{melt}, and the duration of the melt period. As independent field measurements of the components are subject to errors, a residual of the energy balance or closure term C can remain. The measurement setup and the expected margins of error are described in detail in the following paragraphs.

3.1 The Radiation balance

The net radiation budget is the most essential term in the surface energy balance and can be written as

$$Q_{net} = Q_{S\downarrow} - Q_{S\uparrow} + Q_{L\downarrow} - Q_{L\uparrow}, \quad (2)$$

where $Q_{S\downarrow}$ and $Q_{S\uparrow}$ are the incoming and outgoing short-wave components and $Q_{L\downarrow}$ and $Q_{L\uparrow}$ the incoming and outgoing long-wave components, respectively. Using the surface albedo α and Stefan-Boltzmann law, the radiation balance can also be rewritten as

$$Q_{net} = Q_{S\downarrow}(1 - \alpha) + \epsilon Q_{L\downarrow} - \epsilon\sigma T_{surf}^4, \quad (3)$$

where ϵ is the surface emissivity, T_{surf} the surface temperature and σ is the Stefan-Boltzmann constant. In the present study, a variety of sensors is used to determine the radiation components. The net radiation Q_{net} is measured with the NR-Lite (Kipp & Zonen, The Netherlands) net radiation sensors mounted in 1.5 m height. Additional net radiation measurements (CNR1, Kipp & Zonen, The Netherlands) with higher accuracy are available during mid summer 2007 and for the entire observation period of 2008. The CNR1 four component sensor separately measures all radiation balance components. The sensor is located in the vicinity of the eddy-covariance station and is mounted on a 2 m mast (Fig. 1). Further net radiation measurements with an NR-Lite sensor are conducted at a thermokarst pond, which is approximately 0.8 m deep. These additional measurements are performed to investigate differences in the radiation balance between the tundra surface and shallow water bodies, which are a frequent landscape element (Fig. 1). The evaluation of the accuracy of the employed

TCD
4, 901–947, 2010

net radiation sensors is difficult, since World Meteorological Organization (WMO) quality standards are not available for net radiation sensors. Studies comparing the employed sensors with high-accuracy single component sensors (Brotzge and Duchon, 2000; Kohsiek et al., 2007) suggest a relative measurement accuracy of about 20% for the NR-Lite and about 10% for the CNR1 sensor. A sensor comparison under field conditions shows that daily averages of the NR-Lite sensor are about 5 to 10 Wm^{-2} lower compared to the values obtained by the four component sensor. This bias is in most cases within the assumed error margins, but becomes significant under conditions of low net radiation. In addition to the net radiation sensors, measurements of the upwelling thermal radiation (CG1, Kipp & Zonen, The Netherlands) are available at the standard climate tower (Fig. 1), while spatial differences are measured with distributed infrared surface temperature sensors (IRTS-P, Apogee Instruments, USA). The infrared sensors are mounted on small tripods about 0.8 m above the surface and are directed on different tundra soils. According to instrument specifications, the IRTS-P sensors deliver surface temperatures with an accuracy of about 0.5 °C, from which we infer the upwelling thermal radiation following Stefan-Boltzmann law (compare Eq. 3). We assume emissivities ϵ of 0.98 for wet and 0.96 for dry tundra surfaces (Langer et al., 2010a). In order to obtain a more differentiated picture of the short-wave radiation balance, spatially distributed albedo measurements are conducted with a mobile short-wave radiation sensor (SP1110, Skye Instruments, USA). The albedo measurements are conduced during solar noon under clear-sky conditions to obtain a maximum accuracy.

3.2 Turbulent heat fluxes

The turbulent fluxes of momentum, u_*^2, sensible heat, Q_H and latent heat, Q_E, are determined with the eddy covariance method. The applied eddy covariance system consists of a Campbell C-SAT 3D sonic anemometer and open path LICOR LI-7500 CO_2 and H_2O gas analyzer mounted on a 2.4 m mast. The data are sampled at a rate of 20 Hz using a Campbell CR3000 data logger. Sonic anemometer measurements

TCD
4, 901–947, 2010

are conducted during the entire observation period, while the gas analyzer is operated only during the field campaigns, when a reliable power supply and regular maintenance can be accomplished. The eddy-covariance method is based on high-frequency measurements of the sonic temperature T_s, the specific humidity q, the horizontal and vertical wind speed components u and w. Using Reynolds decomposition, the turbulent flux components can be evaluated from the covariances $\overline{u'w'}$, $\overline{T_s'w'}$ and $\overline{q'w'}$ of the fluctuations u', w', T_s' and q' around the average values of the above quantities as

$$u_*^2 = \overline{u'w'}, \tag{4}$$

$$Q_{HB} = \rho_{air}\, c_p\, \overline{T_s'w'}, \tag{5}$$

$$Q_H = \rho_{air}\, c_p\, \overline{T'w'} = \rho_{air}\, c_p\, (\overline{T_s'w'} - 0.51\, \overline{T}\, \overline{q'w'}), \tag{6}$$

$$Q_E = \rho_{air}\, L_{lg}\, \overline{q'w'}, \tag{7}$$

where Q_{HB} denotes the buoyancy flux, c_p the specific heat capacity of air at constant pressure and L_{lg} the specific latent heat of vaporization of water. Note that in the case of measurements over a frozen (snow) surface, L_{lg} must be replaced by the latent heat of sublimation L_{sg}. The buoyancy flux Q_{HB} differs from the true sensible heat flux Q_H due to the difference between the measured sonic and the real air temperature T_s=T (1+0.51q). Hence, the covariance $\overline{T'w'}$ must be corrected according to Eq. 6, if measurements of the specific humidity q are available (Schotanus et al., 1983). As the LICOR gas analyzer is not operated continuously (see above), this correction cannot be applied during parts of the spring and summer period in 2007. The error induced by interpreting the buoyancy flux as sensible heat flux can be estimated using the Bowen ratio, Q_H/Q_E. For Bowen ratios of approximately 0.5 and average air temperatures of $\overline{T}\approx$300 K, the offset is on the order of 15%, which constitutes an additional error during the respective periods. The turbulent fluxes are calculated for 30 min intervals with the internationally standardized "QA/QC" software package "TK2" (Mauder and Foken,

TCD
4, 901–947, 2010

2004; Mauder et al., 2007), which includes all "state-of-the-art" corrections and tests. The quality assessment follows the scheme of Foken et al. (2004), which is based on tests for stationarity of the turbulence and the integral turbulence characteristic (ITC). In this study, the latter is not applied, since the quality criterion of the integral turbulence characteristic is not well defined in arctic region, where stable atmospheric stratification and intermittent turbulence are common (Lüers and Bareiss, 2009). The stationarity criterion is considered to be sufficiently fulfilled (quality flags 1 and 2), if the average covariance inferred from 5 minute subintervals do not deviate more than 30% from the covariance value over the entire 30 min interval (Foken et al., 2004). A graduation of the deviation is used as a quality measure, expressed with quality flags between 1 and 9. In this study, we accept sensible heat fluxes, if both the quality flags of $\overline{u'w'}$ and $\overline{T_s'w'}$ feature quality values of 6 or better. For the latent heat fluxes Q_E, we use the quality flags of $\overline{u'w'}$ and $\overline{q'w'}$, respectively. This quality standard is recommended for long-term observations (Foken and Wichura, 1996). In other field experiments, this quality level is found to be associated with a relative measurement accuracy of about 15% (Mauder et al., 2006), which we assume as the general accuracy of the obtained turbulent heat fluxes. The quality assessment causes a data reduction of about 3% for the sensible and about 4% for the latent heat fluxes. A further data reduction of about 14% originates from the exclusion of the wind sector between 263° to 277°, which is considered to be the lee area of the measurement setup. In order to obtain the magnitude of the latent heat fluxes, when measurements of the LICOR gas analyzer are not available, we use a model approach based on the parametrization of turbulent fluxes introduced by Høgstrøm (1988). The required parameters, such as roughness lengths and surface resistance to evaporation, are determined by model optimization to available measurements. A detailed description of the used model is given in Appendix D. An overview of the available dataset is given in Table 2, where the modeled latent heat fluxes are marked.

Large-scale differences in the distribution of wet and dry tundra patches as well as shallow ponds potentially create differences in the turbulent heat fluxes on the

TCD
4, 901–947, 2010

landscape scale. It is therefore unclear whether the turbulent heat fluxes obtained at a single location are representative on the landscape scale. The impact of such surface heterogeneities on the turbulent heat flux characteristics is evaluated by a second eddy covariance system during the summer of 2008. The second system is identical to the first one and is used as a mobile station, which is moved in a weekly interval along a 1 km east-west transect across the study site (Fig. 1) while the first system provides simultaneous measurements at the reference location. The flux source area of each half-hour value is determined with the footprint model of Schmid (1994). For the footprint calculations, we assume a constant roughness length $z_0=10^{-3}$ m, which we directly infer from the turbulence measurements under neutral atmospheric stratification (Foken, 2008). This value is consistent with typical roughness lengths reported for short grassland (Oke, 1987; Foken, 2008). The fractions of wet and dry tundra areas as well as polygonal ponds for eddy footprint areas are derived from aerial photographs using supervised classification based on field mapping. The locations of the stationary and the mobile eddy system feature differences in average surface soil moisture according to differences in the polygonal structures. The blending height l_b can be approximated by $l_b \approx L_x/200$ (Garratt, 1994), where L_x is the horizontal scale of heterogeneity. With an approximate size of 20 m of the polygonal surface elements, the measurement height of 2.4 m is well above the blending height, so that the obtained flux values can be considered a spatial average of the footprint areas.

3.3 Ground heat flux

The ground heat flux is essential for permafrost, since it determines the annual active layer dynamics as well as the long-term thermal stability of the permanently frozen ground. In this study we apply two different methods to determine the ground heat flux on different time scales.

TCD
4, 901–947, 2010

3.3.1 Calorimetric method

The calorimetric method is used to evaluate the average ground heat flux over longer periods (Appendix B). The method is based on soil temperature and moisture measurements and calculates the average ground heat flux from changes in the sensible and latent heat content of a soil column. The method has been successfully applied in several permafrost regions and is described e.g. by Boike et al. (1998) and Westermann et al. (2009). We use a measurement setup consisting of an active layer temperature and moisture profile to a depth of 0.5 m, which features 5 thermistors (107-L, Campbell Scientific, USA) and 5 Time-Domain-Reflectometry (TDR) soil moisture probes (CS610-L, Campbell Scientific, USA). The calorimetric methods requires temperature measurements to a depth, where no temperature changes occur in the considered time interval (Appendix B). The temperature profile to the depth of zero annual amplitude (15m) are measured in a 26 m bore-hole with a temperature chain featuring 24 thermistors (XR-420, RBR Ltd., Canada).

3.3.2 Conductive method

The conductive method is primarily used to evaluated the diurnal course of the ground heat flux through the upper most ground surface Westermann et al. (2009). Depending on the surface conditions, the ground surface is either defined as the soil or the snow surface. This method directly calculates the heat flux through the soil surface by solving the differential equation of conductive heat transport (Appendix C), which involves the determination of the thermal conductivity of the soil using shallow temperature profile measurements. As the conductive method is not feasible during periods, when a phase change of water occurs, we exclude the transition periods in spring and fall from such calculations. The employed temperature profiles are installed between the surface and about 30 cm depth in different soil substrates, and consist of at least three thermocouples or thermistors with accuracies better than 0.2 K. The instrumented soil substrates are classified as dry, wet and saturated peat soils (Table 1). The sensors

TCD
4, 901–947, 2010

of each profile are placed in soil layers considered to be homogeneous in composition according to visual examination. Furthermore, we assume constant thermal properties over the considered time intervals (Appendix C), which is a good assumption for wet and saturated soils.

During early spring, the heat flux through the snow cover can be calculated using a similar approach. The determination of the snow thermal properties is based on measurements of the snow density and of temperature profiles in the snow conducted in spring 2008. The boundary conditions for the heat flux calculations are obtained from a infrared surface temperature sensor and a thermistor located at the soil-snow interface. Snow heat fluxes are calculated for periods of constant snow depth, which is measured with a ultrasonic ranging sensor (SR50, Campbell Scientific, USA) located next to the measurement setup. The obtained snow heat fluxes must be considered a rough approximation, since the assumption of constant thermal snow properties may be violated in reality (e.g. Sturm et al., 1997; Zhang, 2005).

3.3.3 Soil and snow parameters

Both methods of ground heat flux calculations require knowledge about the thermal properties of soil or snow (compare Appendix B, C). The heat capacity is an essential parameter, which we infer from soil component analyses of soil samples taken during the field campaigns and in situ water content measurements. We assume an error of 10% on each soil fraction, such as water content, ice content and solid soil matrix. A bulk heat capacity of $2.3 \pm 0.3\,\mathrm{MJ\,m^{-3}\,K^{-1}}$ is used for the solid soil fraction. The obtained soil properties and the associated heat capacities are depicted in Table 1. It is evident, that large uncertainties in heat capacity occur at the dry peat soils, since already small variations in the soil composition induce errors of about 60%. As a consequence, we do not evaluate soil heat fluxes at dry locations. The conductive method allows to determine further soil properties, such as the thermal diffusivity and the heat conductivity (Appendix C), which are displayed in Table 1. For wet tundra soils, the obtained diffusivity values show variations in the range of 20%, which results

TCD
4, 901–947, 2010

in a combined error of about 30% for the heat conductivity. A similar error range is calculated for the snow heat conductivity, which we infer from snow density and snow temperature profile measurements using the conductive method (see Appendix C). For simplicity, we assume an error of 30% as appropriate for all ground heat flux calculations, which is about 10% larger than the errors assumed for the other energy balance components.

3.4 Ancillary measurements

Measurements of air temperature and relative humidity (MP-100, Rotronic, Switzerland) are performed at the standard climate tower in the vicinity of the eddy covariance system (Fig. 1). The snow melt during spring is evaluated based on ultrasonic ranging sensors (SR50, Campbell Scientific, USA) located at the standard climate station and the polygonal pond. In addition, we approximate the evolution of snow free areas during the ablation period by automatic daily photographs of the measurement site. The latent heat content of the snow cover E_{melt} is inferred from spatially distributed measurements of the snow-water equivalent immediately before the onset of snow melt in 2008. With an almost identical snow depth, a similar snow-water equivalent is assumed for 2007.

4 Results

4.1 Seasonal energy balance characteristics

The time span considered in this study ranges from April until September of the years 2007 and 2008. For the description of the seasonal energy balance characteristics, we separate the observation period into three subsections according to the specific seasonal climate conditions. The segmentation of the observation period follows broad synoptic changes, such as the presence of snow, the general air temperature evolution and the occurrence of frost events. While the resulting segmentation is unequally

TCD
4, 901–947, 2010

spaced, we provide an equally spaced overview over the seasonal energy balance in Fig. 5. In the following paragraphs, we also examine inter-annual differences in the surface energy balance.

4.1.1 Spring (1 April–31 Mai)

During the spring period, the daily average air temperatures increase strongly from −16 °C to 6 °C in 2007 and from −25 °C to 2 °C in 2008, with notable differences between both years. The increasing temperatures are accompanied by steadily increasing short-wave radiation after the end of the polar night and the shrinking snow cover towards the end of the period. According to the ultrasonic snow depth sensor, the early spring snow depths are in the range from 0.30 and 0.35 m in both years. These point values are confirmed by spatially distributed snow water equivalent measurements in 2008, which yield an average snow depth of about 0.30 m with an average snow density of 190 kg m^{-3}. The onset and course of the snow melt are almost identical for both years. While the snow melt starts in the mid of May shortly after the beginning of the polar day, it typically does not occur in a single event, but is interrupted by declining air temperatures and subsequent snowfall. The first snow melt event last only a few days (10–19 May 2007/10–14 May 2008), during which the elevated polygonal rims become partly snow-free (Fig. 2). The subsequent snow fall delivers only a few centimeters of additional snow cover, which disappear quickly in the second and final melt event (22–30 May 2007/21–29 May 2008). In the following, we refer to the period before the onset of melting as the pre-melt period, while the subsequent time is denoted the snow melt period. The average radiation budget is positive during the entire spring period and of similar magnitude in both years (Fig. 5). Before the onset of snow melt, the diurnal cycle of the net radiation ranges from −40 to 50 Wm^{-2}, but increases significantly after the snow cover has disappeared. This rapid change in the radiation budget is related to the drastic change of the surface albedo, which is about 0.8 before and 0.2 after snow melt. This change in the surface characteristics is reflected in all energy balance components, which we depict in Fig. 2. The turbulent sensible heat flux ranges

TCD
4, 901–947, 2010

from −30 to 20 W m^{-2} during the pre-melt period and basically follows the course of the surface radiation budget. About two days before the onset of snow melt, persistent negative sensible heat fluxes are observed, which appear to be partly decoupled from the net radiation (Fig. 2). The snow surface temperature approaches 0 °C around noon. This relation indicates that both the turbulent sensible heat fluxes as well as the incoming short-wave radiation contribute to the snow melt. As soon as snow free areas are present, the sensible heat flux rapidly exceeds values of 40 W m^{-2}. After the snow cover has disappeared entirely at the end of May, the sensible heat flux reaches peak values of 90 W m^{-2}. A similar evolution is observed for the latent heat flux, which is between 0 and 10 W m^{-2} before the onset of snow melt and quickly increases to values of 50 W m^{-2} during the first snow melt event. After the final melt period, the latent heat flux exceeds values of 100 W m^{-2} and features an average value of 35 W m^{-2} during the last ten spring days of 2008. This average heat flux corresponds to 30 MJ m^{-2} or to 12 mm of evaporated water, respectively. As the snow water equivalent of 2008 amounts to approximately 57 mm, about 20% of the snow cover sublimate or evaporate during the last spring days. Hence, the snow cover effectively supplies 45 mm to the summer time water budget, which constitutes about 20% of the precipitable water of the entire observation period. Considering similar snow heights and the identical course of the ablation process, a similar magnitude of snow cover contribution to the water balance can be assumed in 2007.

The atmospheric stratification is reflected in the stability parameter ζ, which is essentially zero during neutral conditions, larger than zero for stable and smaller than zero for unstable atmospheric stratifications. During the pre-melt period, the atmospheric stratification changes frequently between stable and unstable conditions (Fig. 2). At this time, neutral stratifications occur occasionally in conjunction with wind speeds larger than 2 m s^{-1}. With the onset of snow melt, the wind speed is generally high and the atmospheric stratification becomes essentially neutral (Fig. 2). The average ground heat flux during the spring period is remarkably positive and dominated by storage of sensible heat in both years (Table 2), which is associated with a steady warming of the

TCD
4, 901–947, 2010

deeply frozen soil. A closer look at the evolution of the ground heat storage (Fig. 3) reveals a faster soil warming in early spring 2007. This difference in the evolution of the ground heat budget compared to 2008 is related to significantly warmer air and snow surface temperatures, but relatively cold soil temperatures in early spring 2007 (Table 2). In both years, the amplitude of the ground heat flux through the snow cover typically ranges from −20 and 20 $W m^{-2}$ during the pre-melt period and is thus in the range of the turbulent sensible heat fluxes.

4.1.2 Summer (1 June–31 August)

The summer period is characterized by a strong short-wave radiative forcing, a snow-free surface, day time temperatures well above the freezing point and the thawing of the active layer (Fig. 5, Table 2). Polar day conditions last until 7 August, featuring high values of incoming short-wave radiation. Daily averages of incoming short-wave radiation frequently exceed values of 300 $W m^{-2}$ under clear-sky conditions and can be as low as 20 $W m^{-2}$ under overcast situations, which occur frequently. The reduced solar radiation during cloudy conditions is partly compensated by the thermal sky radiation, which is then significantly increased. The daily average of incoming long-wave radiation typically ranges from 280 $W m^{-2}$ for clear-sky and 380 $W m^{-2}$ for cloudy situations. The daily average of emitted long-wave radiation varies between 330 $W m^{-2}$ and 420 $W m^{-2}$, which corresponds to average surface temperatures of 3 and 20 °C. Consequently, the net long-wave losses frequently exceed 100 $W m^{-2}$ during clear-sky conditions, while they are almost zero during overcast situations. The average summer net radiation of 2007 is slightly higher compared to 2008 (Fig. 5), which is most likely caused by differences in cloudiness. This is also confirmed by the precipitation rates, which are doubled during the early summer period of 2008.

In both years, unstable stratifications ($\zeta<0$) occur frequently during the day, but usually do not last longer than 12 h. The nights are dominated by neutral stratifications ($\zeta\approx0$), while stable atmospheric conditions ($\zeta>0$) are only observed occasionally under calm conditions and highly negative values of the net radiation. The turbulent heat

TCD
4, 901–947, 2010

fluxes constitute dominant components in the summer time energy balance. About 20 to 30% of the available radiative energy is consumed by turbulent sensible heat flux, while evapotranspiration amounts to about 40 to 50% (Fig. 5, Table 2). The turbulent heat fluxes show a strong diurnal cycle and frequently exceed values of 130 W m^{-2} for the sensible and 150 W m^{-2} for the latent heat flux during the day. During the night, significant negative sensible heat fluxes on the order of −20 W m^{-2} are observed, while negative latent heat fluxes (dew fall) occur only occasionally. Such events are then associated with a highly negative net radiation and low surfaces temperatures, as they occur at the end of the summer section. We depict an exemplary period during late summer 2008 in Fig. 4, which illustrates the typical diurnal cycle of the heat flux components forced by the incoming solar radiation. The wind speed appears to be associated with a diurnal pattern (Fig. 4), which indicates enhanced turbulent heat exchange during the day and lowered turbulence during the night. A dependence of the wind direction on the day time is not detected. For both years, the average Bowen ratio Q_H/Q_E is essentially below zero and indicates high rates of evapotranspiration. The amount of evaporated water is about 70 mm in 2007 and about 100 mm in 2008, which is about the same as the precipitation measured in the concerned sub-periods (Table 2).

When comparing the turbulent heat fluxes for the two years, it must be emphasized that the average flux values depicted in Table 2 are based on different sub-periods and are not directly comparable. For the inter-annual comparison, we make use of modeled latent heat flux values. The gap-filled energy balance with equally spaced averaging intervals is illustrated in Fig. 5. Inter-annual differences in the turbulent heat fluxes occur during the early and mid summer period, when the net radiation budget of 2008 is also affected by clouds. The reduced radiation budget results in generally decreased sensible heat fluxes, while the latent heat fluxes appear to be slightly increased during early summer 2008. In both years, the ground heat flux is a remarkable term in the summertime energy balance, which consumes about 20 to 25% of the available radiation budget. The ground heat flux is characterized by active layer thawing, which makes up 60% of the entire ground heat flux (Fig. 3). The remaining fraction

TCD
4, 901–947, 2010

is stored as sensible heat in the deeper soil. With a high soil water content of about 70%, a maximum thaw depth of only 0.40 m is reached during the summer period. The shallow thaw depth causes strong soil temperature gradients in the active layer, which enhance the ground heat flux. The ground heat flux shows a strong diurnal cycle and frequently exceeds values of 50 W m^{-2} during the day (Fig. 4), while negative ground heat fluxes are observed only occasionally during clear-sky nights.

4.1.3 Fall (1 September–30 September)

We denote a short transition period as fall segment, which in both years is characterized by steadily decreasing air and surface temperatures, the onset of freezing and occasional snow fall, while a continuous snow cover does not form yet. In both years, the fall period starts with air and surface temperatures well above the freezing point and ends with temperatures around 0 °C. Only occasional freezing events are observed during the fall period 2007, while sustained freezing already occurs in 2008. The interannual difference in the temperature evolution is reflected in the average air and surface temperatures, as well as in the ground heat fluxes (Table 2). In 2008, the entire active layer already approaches temperatures of 0 °C at 17 September, but warms again for one week, before the soil temperatures finally reach the zero-curtain around 25 September. In contrast, the soil temperature in 2007 never enters the zero-curtain during the fall period. Hence, the average ground heat flux in 2007 only indicates positive sensible heat storage (Table 2), which is caused by the delayed warming of soil in a depth of 1 to 10 m, which in 2008 is almost equal to the released latent heat from the initial freezing (Table 2). The average radiation budget is significantly reduced, but still positive in both years and features a distinct diurnal cycle with daytime values on the order of 100 W m^{-2}. A negative net radiation on the order of −50 W m^{-2} is frequently observed during the nights in 2008, which occurs only sporadically in 2007. Contrary to the summer segment, the reduced radiative losses during the nights and the significantly higher amount of precipitation indicate an increased cloudiness in fall 2007 (Table 2). The average atmospheric sensible heat flux is directed towards the surface in

TCD
4, 901–947, 2010

both years, but is more negative in 2008. This corresponds to the pronounced negative night time temperature gradients (T_{surf}–T_{air}) in 2008. Despite the reduced net radiation, the latent heat fluxes still play a dominant role in the surface energy balance (Fig. 5). Almost 50% of the net short-wave radiation is consumed by evapotranspiration, which corresponds to the amount of precipitation during the fall section. The atmospheric stratification in both years is dominated by neutral conditions, corresponding to high wind speeds. However, occasional events of stable stratification occur during calm nights, when the radiation budget becomes highly negative and strong temperature gradients in the atmospheric boundary layer arise. In accordance with the described inter-annual differences in the energy balance evolution, such events are observed more frequently in 2008. In both years, the energy balance closure term C is relatively high (Table 2). This high closure term can be partly explained by an underestimation of the net radiation: a comparison of the NR-Lite and the four component sensor during fall 2008 reveals an offset of 6 W m^{-2}, which is substantial considering the generally low radiation budget.

4.2 Spatial energy balance variability

The polygonal tundra features pronounced micro-scale heterogeneity, regarding the surface moisture and vegetation cover. The elevated polygonal rims are typically covered with dry mosses, while the lowered centers are filled with wet peat soils or shallow ponds. Considering these surface heterogeneities, spatial differences in the energy balance are likely to occur. Spatially distributed albedo measurements yield typical values in the range of 0.2 for dry and 0.15 for wet tundra surfaces. The latter value is consistent with the average albedo of 0.14 obtained from measurements of the four component radiation sensor, which is directed towards a wet tundra spot. During local noon and clear-sky conditions, the typical surface temperature differences between dry and wet locations are on the order of 5 to 10 °C, which indicates increased radiative losses at the dry and warm surfaces. During the nights and during overcast periods, the spatial differences in the surface temperature and thus the radiation budget largely

TCD
4, 901–947, 2010

vanish. However, sustained differences in the net radiation budget exist between the tundra soil and the polygonal pond (Fig. 6). During the pre-melt period, the net radiation at the polygonal pond is constantly 5 to 10 W m^{-2} lower compared to the tundra surface. After the melt period, the measurements show a significantly higher net radiation at the water body on the order of 20 to 30 W m^{-2}, which gradually diminish in the course of the summer season (Fig. 6).

Spatial differences in the turbulent heat fluxes are examined for an exemplary situation at the second location of the mobile eddy system. According to the footprint analysis, the second mobile eddy station features a 20% higher fraction of dry surface area than the reference location (Fig. 1). The simultaneous measurements at both location indicates that moderate spatial differences on the order of 20 W m^{-2} (10–20%) can be expected for the sensible and latent heat fluxes under conditions of high radiative forcing ($Q_{net} > 200$ W m^{-2}) (Fig. 7), which occur only sporadically during the summer period (Fig. 7). During the fall period, when the radiation balance is further reduced, almost no spatial differences in sensible and latent heat fluxes are measured along the transect.

5 Discussion

5.1 Data quality

The quality of the energy balance measurements can be evaluated according to the energy balance ratio (Wilson et al., 2002)

$$\mathrm{EBR} = \frac{Q_H + Q_E}{Q_{net} - Q_G}, \quad (8)$$

which in the case of a closed energy balance (C=0) is unity. The EBR distribution contains information about the characteristics of the errors of the energy balance measurements, such as the presence of systematic and random errors. Since the EBR is highly

TCD
4, 901–947, 2010

sensitive to measurement errors during situations of low heat fluxes, we only consider measurements conducted during conditions of $Q_{net} \leq -30\,W\,m^{-2}$ and $Q_{net} \geq 30\,W\,m^{-2}$. The normalized EBR distribution of the entire data set roughly resembles a normal distribution featuring a mean value of 0.86, a standard deviation of 0.34, and a slightly positive skewness of 0.47 (Fig. 8). If only random measurement errors would be involved, the expected EBR distribution should be more similar to the normal distribution displayed in Fig. 8. This distribution is calculated assuming a relative error of 15% for Q_H+Q_E (see Sect. 3.2) and 20% for $Q_{net}-Q_G$ (see Sect. 3.1), which results in a standard deviation of 0.25. The measured EBR distribution suggests that the energy balance is systematically not closed by about 15%, which is potentially caused by a negative bias of the turbulent heat fluxes or a positive bias of the term $Q_{net}-Q_G$. The latter is not likely since the employed net radiation sensor (NR-Lite) slightly underestimates the radiation budget (compare Sect. 3.1), while the ground heat flux would have to be unrealistically small to cause a positive bias of $Q_{net}-Q_G$. The shape and width of the measured EBR distribution is similar to the normal distribution, which suggests that the assumed error margins of the energy balance components are realistic.

5.2 Controlling factors in the energy balance

Three factors can be identified that essentially determine the energy balance characteristics at the investigated wet tundra landscape. The determining factors are (i) the snow cover, (ii) the presence or absence of a cloud cover and (iii) the thermal state of the permafrost.

(i) Although the snow cover is only shallow at the study site, it has strong implications for the surface energy balance. Firstly, the albedo of the snow cover is about a factor of four higher than the albedo of the snow-free tundra surface. Secondly, the thermal conductivity of snow is about a factor of two lower than the thermal conductivity of frozen peat. The second point is of particular importance during winter, when the low thermal conductivity of the snow cover impedes the release of

TCD
4, 901–947, 2010

energy from the ground and leads to a reduced ground heat flux (see Langer et al., 2010b). During spring, however, the soil has already cooled out, so that the lower thermal conductivity of the snow is of minor importance for the ground heat budget and the surface energy balance (Goodrich, 1982). In contrast, the high albedo of the snow has a strong impact on the surface energy budget during the spring period, when the incoming short-wave radiation already features high values. At the study site, the snow cover effectively reduces the net short-wave radiation until the beginning of the polar day period. The melting of the snow cover with the associated change in surface albedo triggers a sudden change from a winter to a summer surface energy balance, so that the timing of snow melt is a critical point in the annual course of the surface energy balance. In both investigated years, the timing of the snow melt is almost identical. Iijima et al. (2007) point out that snow cover disappearance in eastern Siberia is strongly related to the attenuation of the Siberian-High with subsequent advection of warm and moist air masses from the west. According to the distinct contribution of sensible atmospheric heat flux to the snow melt, our measurements indicate the presence of warm air masses. However, we identify the short-wave radiation as the dominant factor in the snow melt process. We emphasize that the correct representation of the snow melt must be considered crucial in permafrost modeling. It is therefore highly desirable to gather a better understanding of the triggering processes of the snow melt and their representation in models.

(ii) The large-scale advection of warm air is usually related to increased cloudiness, which essentially alters the surface radiation budget and the prevailing surface and air temperature conditions. During the spring period, our results indicate that the observed inter-annual differences in the ground temperatures are caused by different air temperatures, which are presumably related to the general synoptic conditions. During the summer months, the net radiation is essentially reduced for cloud-covered skies, which leads to an effective surface cooling. During the summer months, the cloud cover has an impact on the turbulent heat fluxes, while

TCD
4, 901–947, 2010

the ground heat budget is only marginally affected. Since the average surface temperature is not drastically reduced by the increased cloud cover the active layer thawing is only slightly affected. During the fall period, the contrary effect of a cloud cover is observed, as clouds reduce the long-wave radiative losses, which in turn leads to increased surface temperatures. The impact of clouds on the ground heat budget is observed to be largest during the fall season, when increased cloudiness significantly delays the refreezing process in 2007, while the average air temperatures are similar. This ambiguous influence of the cloud cover on the surface radiation budget in the Arctic is confirmed in several studies (Curry et al., 1996; Intrieri et al., 2002; Shupe and Intrieri, 2004).

(iii) During the entire observation period, the ground heat flux is an essential component in the surface energy balance. About 20% of the net radiation is stored as latent and sensible heat in the ground, which is in the upper range of typical values reported for other arctic permafrost regions (Boike et al., 1998; Lynch et al., 1999; Eugster et al., 2000; Westermann et al., 2009). The high contribution of the ground heat flux to the surface energy balance is clearly caused by the cold permafrost temperatures, the shallow active layer depth and the large annual surface temperature amplitude, which is related to the continental climate conditions. Due to the low permafrost temperatures, the sensible heat storage makes up about 50% of the entire ground heat flux. This clearly limits the value of the widely used Stefan equation, that evaluates the active layer dynamics by assuming the ground heat flux to be entirely used for thawing. As the contribution of the ground heat flux to the surface energy balance is significant even in the summer months, an adequate representation of the soil domain in global climate models seems mandatory, if the land-atmosphere exchange processes in permafrost regions are to be modeled correctly. This issue is of particular importance, as permafrost areas with continental climate, where a significant contribution of the ground heat flux can be expected, occupy vast areas in the Arctic. The improvement of modeling results by employing more realistic parameterizations of the soil processes

TCD
4, 901–947, 2010

has been outlined in a number of studies (e.g Peters-Lidard et al., 1998; Cox et al., 1999; Viterbo et al., 1999; Pitman, 2003). In the second part of this study (Langer et al., 2010b), the representation of the soil and particularly of soil freezing processes in models is discussed in more detail.

5.3 Spatial differences of the surface energy balance

In this study, spatial differences in the surface energy balance are observed for (i) the radiation budget and (ii) the turbulent fluxes.

(i) With albedo differences between wet and dry areas on the order of 0.05, the net short-wave radiation can be on average by up to 7 W m^{-2} higher at wet compared to dry areas, while the differences can exceed 25 W m^{-2} for high radiative forcing during midday. This difference is further contrasted by the higher surface temperatures of dry surfaces, which can be about 5 K warmer than wet surfaces during conditions of high radiative forcing. It is therefore conceivable, that the net radiation balance at wet and dry locations can deviate up to 50 W m^{-2} from each other. This difference is partly attenuated during the night, when the wet surfaces are warmer and the short-wave forcing is nonexistent or negligible. Moreover, due to the rare occurrence of high values of net radiation we assume that the average differences in net radiation between wet and dry areas does not exceed 10 W m^{-2}. More pronounced spatial differences in the radiation balance are measured between the tundra and water bodies. The net radiation of the investigated pond is slightly lower in frozen conditions during spring, but significantly higher during the summer months. Albedo differences during spring are not likely, since all surfaces are covered by snow, so that the measured differences in the radiation budget are most likely explained by increased surface temperatures at the frozen pond during spring. During the summer period, almost similar average surface temperatures are observed for the water body and the tundra surface (see Langer et al., 2010b). Hence, the differences in net radiation are most likely explained by a lower albedo

TCD
4, 901–947, 2010

of the water body. The pond investigated in this study indicates that small shallow water bodies can have a significant influence on the radiation budget in polygonal tundra landscapes, as they are frequent landscape elements. While the impact of larger water bodies on the arctic climate conditions has been investigated (Krinner, 2003; Rouse et al., 2005; Krinner and Boike, 2010), such small water bodies have not received similar attention. It is thus highly desirable to evaluate the impact of small water bodies on the larger-scale surface energy balance, particularly since such micro-scale landscape structures usually remain undetected in remote sensing applications and are neglected in model approaches. In the second part of this study (Langer et al., 2010b), the winter aspect of the surface energy balance of small ponds is addressed in more detail.

(ii) Micro-scale differences of the turbulent fluxes are verified by the mobile eddy covariance system. The measurements reveal differences in sensible and latent heat fluxes according to variations in the fractions of dry and wet surfaces in the footprint areas (Fig. 4). The observed spatial variations are caused by the small scale surface temperature differences between wet and dry areas. As the temperature difference between wet and dry surfaces depends on the net radiation budget, significant differences in the turbulent fluxes are limited to clear-sky situations, which only occur occasionally during the summer period. Since the long-term averages of the turbulent heat fluxes are almost equal for the stationary and the mobile eddy covariance system, we conclude that the presented sensible and latent heat fluxes are representative on the landscape scale.

TCD
4, 901–947, 2010

6 Conclusions

In this study we present a comprehensive surface energy balance study of at wet polygonal tundra landscape from April to September (2007–2008) considering seasonal and spatial variations. This comprehensive study improves the understanding of the energy exchange processes at soil-atmosphere interface of a typical permafrost landscape. The obtained results can be of great value for the improvement and development of permafrost model schemes, as they are intended to be incorporated in climate models. In particular the following conclusions can be drawn from the obtained results:

- The spring, summer and fall energy balance is dominated by the net radiation. Critical factors for the surface radiation budget are in particular the snow cover and clouds. The timing of snow melt in spring essentially controls the amount of short-wave radiation that is available for energy partitioning. The relevance of the snow cover for the surface radiation budget is further intensified by the presence of almost polar day conditions. The cloud cover has its greatest impact on the ground heat budget during fall, when radiative losses are largely reduced and the refreezing of the tundra is significantly delayed.

- The surface energy balance is essentially affected by the ground heat flux, which is of similar magnitude as the sensible heat flux. The significant ground heat flux is induced by strong temperature gradients in the shallow active layer and in the permafrost body, which are the result of both continental climate and high soil water and ice content.

- The larger scale surface energy balance is significantly affected by the occurrence of small water bodies, which essentially increase the surface radiation budget and the ground heat storage of the tundra landscape during the summer time.

TCD
4, 901–947, 2010

Appendix A

Definitions and constants

Q_{net} – net radiation
$Q_{S\downarrow}$ – incoming short-wave radiation
$Q_{S\uparrow}$ – outgoing short-wave radiation
ΔQ_S – net short-wave radiation
$Q_{L\downarrow}$ – incoming long-wave radiation
$Q_{L\uparrow}$ – outgoing long-wave radiation
ΔQ_L – net long-wave radiation
Q_{HB} – buoyancy flux
Q_H – sensible heat flux
Q_E – latent heat flux
Q_G – ground or snow heat flux
E_{melt} – latent heat content of the snow pack
Q_{melt} – energy flux through melting of the snow pack
C – residual of the energy balance
u – horizontal wind speed
w – vertical wind speed
T_{air} – air temperature
T_s – sonic air temperature
T_v – virtual temperature
q – specific humidity
u_* – friction velocity
z_0 – aerodynamic roughness length
$\zeta = z/L_*$ – stability parameter (z: measurement height, L_*: Obukhov length)
$\kappa = 0.4$ – von Kármán constant
R_H – relative humidity
T_{surf} – surface temperature
α – surface albedo
ϵ – surface emissivity
σ – Stefan-Boltzmann constant

TCD
4, 901–947, 2010

c_p – specific heat capacity of air at constant pressure
ρ_{air} – density of air
$\rho_w = 1.0\,g\,cm^{-3}$ – density of water
$\rho_{ice} = 0.91\,g\,cm^{-3}$ – density of ice
$L_{sl} = 0.33\,MJ\,kg^{-1}$ – specific latent heat of fusion of water
$L_{lg} = 2.5\,MJ\,kg^{-1}$ – specific latent heat of vaporization of water
$L_{sg} = 2.8\,MJ\,kg^{-1}$ – specific latent heat of sublimation of ice
D_h – thermal diffusivity
K_h – thermal conductivity
C_h – volumetric heat capacity
$C_{h,w} = 4.2\,MJ\,m^{-3}\,K^{-1}$ – volumetric heat capacity of water
$C_{h,i} = 1.9\,MJ\,m^{-3}\,K^{-1}$ – volumetric heat capacity of ice
$C_{h,a} \approx 0.001\,MJ\,m^{-3}\,K^{-1}$ – volumetric heat capacity of air
$C_{h,s} \approx 2.3\,MJ\,m^{-3}\,K^{-1}$ – volumetric heat capacity of the solid soil matrix
A bulk heat capacity $C_{h,s}$ is used for the solid matrix, since typical values of organic and mineral soils do not differ more than 20% from each other (compare Sect. 3.3.3)

Appendix B

The calorimetric method

The change of the sensible heat content of a soil volume with area A and depth z with uniform temperature and a constant heat capacity is given by

$$E(t_2) - E(t_1) = A\,z\,C_h\,(T(t_2) - T(t_1)), \tag{B1}$$

where $T(t_1)$ and $T(t_2)$ are the temperatures at times t_1 and t_2. In the case of a temperature dependence of the heat capacity and non-uniform temperature distribution in depth $C_h(T(t,z))$, Eq. B1 must be rewritten to

$$E(t_2) - E(t_1) = A \int_0^z \int_{T(t_1,z')}^{T(t_2,z')} C_h(T')\,dT'\,dz'. \tag{B2}$$

TCD
4, 901–947, 2010

The temperature dependence of C_h is caused by the phase change of water and is calculated as

$$C_h(T) = \theta(T)\, C_{h,w} + (\theta_{max} - \theta(T))C_{h,i} + (1 - P_{dry})C_{h,s}, \quad \text{(B3)}$$

where P_{dry} is the porosity of the soil, θ_{max} is the maximum unfrozen water content, and $\theta(T)$ is the temperature-dependent liquid water content, which is referred to as "freeze characteristic". The volumetric fraction of the solid matrix and thus the porosity is determined from soil samples and the volumetric water and ice content is obtained from in situ TDR-measurements (see Boike et al., 2003, for details). To account for the release or consumption of energy through freezing and thawing, Eq. B2 is extended to

$$E(t_2) - E(t_1) = A \int_0^z \rho_w L_{sl}[\theta(T(t_2,z')) - \theta(T(t_1,z'))]\, dz' + A \int_0^z \int_{T(t_1,z')}^{T(t_2,z')} C_h(T')\, dT'\, dz'. \quad \text{(B4)}$$

This method of ground heat flux determination requires knowledge about the soil-specific freeze characteristics or direct measurements of the soil water content. The employed soil temperature measurements must extend to a depth of constant temperatures during the considered measurement period. If such a deep temperature profile is not available, the heat flux below the measurement depth can be obtained by solving the heat transfer equation at the lower boundary (Eq. C3, see below).

Appendix C

The conductive method

The conductive method makes use of the heat transfer equation to determine the ground heat flux. Firstly, the thermal conductivity of the soil or snow must be evaluated. This procedure requires a time series of soil temperatures measured in a profile at three depths, $T_m(z_1,t)$, $T_m(z_2,t)$ and $T_m(z_3,t)$ with $z_1<z_2<z_3$. The one-dimensional heat transfer equation is written as

$$C_h(t,z)\frac{\partial T(t,z)}{\partial t} = \frac{\partial}{\partial z}K_h(t,z)\frac{\partial T(t,z)}{\partial z} \quad \text{(C1)}$$

TCD
4, 901–947, 2010

where $T(t,z)$ denotes the soil or snow temperature at time t and depth z. Assuming constant heat capacities and thermal conductivities $K_h(t,z)$ in space and time, the one-dimensional heat transfer equation is simplified to

$$\frac{\partial T(z,t)}{\partial t} = D_h \frac{\partial^2 T(z,t)}{\partial z^2} \tag{C2}$$

where $D_h = K_h / C_h$ denotes the thermal diffusivity. The solution of Eq. C2) is obtained by the partial differential equation solver incorporated in MATLAB. The required boundary conditions are given by the outer sensors of the temperature profile, $T_m(z_1,t)$ and $T_m(z_3,t)$. The initial conditions are inferred from linear interpolation between all the three sensors at t=0, which is not critical to the solution, since it becomes independent of the initial temperature state after a few time steps in the shallow soil layer. The numerical solver delivers the temperature distribution of the considered spatial domain, including $T(t,z_2)$, so that the thermal diffusivity D_h can be evaluated by minimizing the least mean square error to the measured temperatures at depth z_2, $T_m(t,z_2)$. We use time series of several days for the determination of the thermal diffusivity of different surface substrates (see Table 1). Note that this procedure assumes homogeneous substrate composition in the considered soil or snow layer, which may not be the case in nature. The heat flux through the upper boundary can be evaluated by

$$Q_G(t) = D_h C_h \left. \frac{\partial T(z,t)}{\partial z} \right|_{z=z_1} . \tag{C3}$$

The conductive methods has been applied by Westermann et al. (2009), while similar concepts are explored by Nicolsky et al. (2009).

Appendix D

Modeling of latent heat fluxes

This model approach is used when eddy covariance measurements of the latent heat flux are not available. The model is based on eddy-covariance measurements of wind speed and sonic temperature and uses ancillary measurements of relative humidity and surface temperature.

TCD
4, 901–947, 2010

The model is based on commonly used parameterizations of the atmospheric transport mechanisms (Foken, 2008), which we shortly describe in the following. According to Monin-Obukhov similarity theory, the latent heat flux can be related to the difference between specific humidity at measurement height $\overline{q}(z_m)$ and roughness length $\overline{q}(z_0)$ by

$$\overline{q'w'} = (\overline{q}(z_m) - \overline{q}(z_0))\, \kappa\, u_* \left[\ln \frac{z_m}{z_0} - \Psi_W \left(\frac{z_m}{L_*}, \frac{z_0}{L_*} \right) \right]^{-1} \quad \text{(D1)}$$

with

$$\Psi_W \left(\frac{z_m}{L_*}, \frac{z_0}{L_*} \right) = \int_{z_0}^{z_m} \frac{1 - \varphi_W(z'/L_*)}{z'} dz', \quad \text{(D2)}$$

where κ denotes the von Kármán constant (0.4), u_* the friction velocity and $\varphi(z/L_*)$ is a universal function (see below). The quotient z/L_* denotes the stability parameter ζ, where L_* is the Obukhov length L_* defined in Eq. D6. Using Eq. D1 and rewriting the turbulent transport terms as atmospheric resistance r_a, the latent heat flux Q_E can be evaluated by

$$Q_E = - \frac{\rho_{air}\, L_{lg}}{r_a + r_s} \left(\overline{q}(z_m) - \overline{q}(z_0) \right), \quad \text{(D3)}$$

with

$$r_a := (\kappa u_*)^{-1} \left[\ln \frac{z_m}{z_0} - \Psi_W \left(\frac{z_m}{L_*}, \frac{z_0}{L_*} \right) \right], \quad \text{(D4)}$$

where ρ_{air} is the density of air, L_{lg} the latent heat of vaporization of water and r_s the surface resistance to evapotranspiration (Garratt, 1994). For calculation over the snow surface L_{lg} must be replaced by the latent heat of sublimation L_{sg}. The specific humidity at the surface $q(z_0)$ is inferred from to the surface temperature T_{surf} using the Magnus formula that delivers the water vapor pressure over a water surface or an ice surface, respectively. During the summer month, the surface is not entirely saturated, and a surface resistance is required to account for the reduced availability of water. We use measured time series of the latent heat flux to fit the surface resistance of summer and fall. We assume the surface resistance to be constant in time. The roughness length z_0 can be inferred from measurements of u_*^2 under neutral atmospheric conditions (Foken, 2008). Note that we assume the aerodynamic roughness length to be the

TCD
4, 901–947, 2010

roughness length of water vapor. The fitting procedure yields a surface resistance of about $50\,s\,m^{-1}$ with a roughness length determined to be 10^{-3} m during the summer period. When the ground is snow-covered, the surface resistance is set to zero, while the roughness is determined to 5×10^{-4} m. The universal universal function Ψ_W is chosen according to Høgstrøm (1988) as

$$\varphi_W(\zeta) = \begin{cases} 0.95\,(1 - 11.6\,\zeta)^{-1/4} & \text{for } \zeta \le 0 \\ 0.95 + 7.8\,\zeta & \text{for } \zeta > 0 \end{cases} \tag{D5}$$

The Obukhov length L_*, which is required for the stability parameter ζ is directly obtained from eddy-covariance measurements using

$$L_* = -\frac{u_*^3 \overline{T}_v}{\kappa\, g\, (\overline{T_v' w'})}, \tag{D6}$$

where g is the gravitational acceleration and T_v the virtual temperature. Note that the virtual temperature T_v is substituted by the sonic temperature T_s (Foken, 2008).

Acknowledgements. We are thankful to the Department of Micro-Meteorology of the University of Bayreuth headed by Thomas Foken for providing the eddy-covariance post-processing software. We are also thankful to Claudia Fiencke and Tina Sanders from the Institute of Soil Science of the University of Hamburg for the soil component analyses. We gratefully acknowledge financial support by the Helmholtz Association through a grant (VH-NG 203) awarded to Julia Boike.

References

Are, F. and Reimnitz, E.: An overview of the Lena River Delta setting: geology, tectonics, geomorphology, and hydrology, J. Coast. Res., 16, 1083–1093, 2000. 905

Boike, J., Roth, K., and Overduin, P.: Thermal and hydrologic dynamics of the active layer at a continuous permafrost site (Taymyr Peninsula, Siberia), Water Resour. Res., 34, 355–363, 1998. 911, 923

TCD
4, 901–947, 2010

Boike, J., Roth, K., and Ippisch, O.: Seasonal snow cover on frozen ground: Energy balance calculations of a permafrost site near Ny-Alesund, Spitsbergen, J. Geophys. Res.-Atmos., 108, 8163–8173, 2003. 929
Boike, J., Wille, C., and Abnizova, A.: Climatology and summer energy and water balance of polygonal tundra in the Lena River Delta, Siberia, J. Geophys. Res.-Biogeo., 113, G03025, doi:10.1029/2007JG000540, 2008. 904, 905
Brotzge, J. and Duchon, C.: A field comparison among a domeless net radiometer, two four-component net radiometers, and a domed net radiometer, J. Atmos. Ocean. Tech., 17, 12, 1569–1582, 2000. 907
Brown, J., Ferrians Jr., O., Heginbottom, J., and Melnikov, E.: Circum-Arctic map of permafrost and ground-ice conditions, US Geological Survey Circum-Pacific Map, 1997. 903, 940
Callaghan, T., Björn, L., Chernov, Y., Chapin, T., Christensen, T., Huntley, B., Ims, R., Johansson, M., Jolly, D., Jonasson, S., et al.: Effects of changes in climate on landscape and regional processes, and feedbacks to the climate system, AMBIO, 33, 459–468, 2004. 903
Christensen, T. and Cox, P.: Response of methane emission from Arctic tundra to climatic change: Results from a model simulation, Tellus B, 47, 301–309, 1995. 903
Christensen, T., Ekberg, A., Ström, L., Mastepanov, M., Panikov, N., Öquist, M., Svensson, B., Nykänen, H., Martikainen, P., and Oskarsson, H.: Factors controlling large scale variations in methane emissions from wetlands, Geophys. Res. Lett., 30, 1414, doi:10.1029/2002GL016848, 2003. 903
Comiso, J.: Arctic warming signals from satellite observations, Weather, 61, 2006. 902
Cox, P., Betts, R., Bunton, C., Essery, R., Rowntree, P., and Smith, J.: The impact of new land surface physics on the GCM simulation of climate and climate sensitivity, Clim. Dynam., 15, 183–203, 1999. 924
Curry, J., Rossow, W., Randall, D., and Schramm, J.: Overview of Arctic cloud and radiation characteristics, J. Climate, 9, 1731–1764, 1996. 923
Davidson, E. and Janssens, I.: Temperature sensitivity of soil carbon decomposition and feedbacks to climate change, Nature, 440, 165–173, 2006. 903
Eugster, W., Rouse, W., Pielke Sr., R., McFadden, J., Baldocchi, D., Kittel, T., Chapin, F., Liston, G., Vidale, P., Vaganov, E., and Chambers, S.: Land-atmosphere energy exchange in Arctic tundra and boreal forest: available data and feedbacks to climate, Global Change Biol., 6, 84–115, 2000. 923
Foken, T.: Micrometeorology, Springer, 2008. 910, 931, 932

TCD
4, 901–947, 2010

Foken, T. and Wichura, B.: Tools for quality assessment of surface-based flux measurements, Agr. Forest Meteorol., 78, 83–105, 1996. 909
Foken, T., Göckede, M., Mauder, M., Mahrt, L., Amiro, B., and Munger, J.: Post-field data quality control, in: Handbook of Micrometeorology: A Guide for Surface Flux Measurement and Analysis, Kluwer, 2004. 909
Garratt, J.: The atmospheric boundary layer, Cambridge Univ. Pr., 1994. 910, 931
Goodrich, L.: The influence of snow cover on the ground thermal regime, Can. Geotech. J., 19, 421–432, 1982. 922
Grigoriev, N.: The temperature of permafrost in the Lena delta basin – deposit conditions and properties of the permafrost in Yakutia, Yakutsk, chap. 2, 97–101 pp., 1960. 905
Hansen, J., Ruedy, R., Sato, M., Imhoff, M., Lawrence, W., Easterling, D., Peterson, T., and Karl, T.: A closer look at United States and global surface temperature change, J. Geophys. Res.-Atmos., 106, 23947–23963, 2001. 902
Hinzman, L., Bettez, N., Bolton, W., Chapin, F., Dyurgerov, M., Fastie, C., Griffith, B., Hollister, R., Hope, A., Huntington, H., et al.: Evidence and implications of recent climate change in northern Alaska and other arctic regions, Climatic Change, 72, 251–298, 2005. 903
Hobbie, S., Schimel, J., Trumbore, S., and Randerson, J.: Controls over carbon storage and turnover in high-latitude soils, Global Change Biol., 6, 196–210, 2000. 903
Høgstrøm, U.: Non-dimensional wind and temperature profiles in the atmospheric surface layer: A re-evaluation, Bound.-Lay. Meteorol., 42, 55–78, 1988. 909, 932
Iijima, Y., Masuda, K., and Ohata, T.: Snow disappearance in Eastern Siberia and its relationship to atmospheric influences, Int. J. Climatol., 27, 169–178, 2007. 922
Intrieri, J., Shupe, M., Uttal, T., and McCarty, B.: An annual cycle of Arctic cloud characteristics observed by radar and lidar at SHEBA, J. Geophys. Res.-Oceans, 107, 8030, doi:10.1029/2000JC000423, 2002. 923
Kohsiek, W., Liebethal, C., Foken, T., Vogt, R., Oncley, S., Bernhofer, C., and Debruin, H.: The Energy Balance Experiment EBEX-2000, Part III: Behaviour and quality of the radiation measurements, Bound.-Lay. Meteorol., 123, 55–75, 2007. 907
Krinner, G.: Impact of lakes and wetlands on boreal climate, J. Geophys. Res.-Atmos., 108, 4520, doi:10.1029/2002JD002597, 2003. 925
Krinner, G. and Boike, J.: A study of the large-scale climatic effects of a possible disappearance of high-latitude inland water surfaces during the 21st century, Boreal Environ. Res., 15, 203–217, 2010. 925

TCD
4, 901–947, 2010

Kutzbach, L., Wagner, D., and Pfeiffer, E.: Effect of microrelief and vegetation on methane emission from wet polygonal tundra, Lena Delta, Northern Siberia, Biogeochemistry, 69, 341–362, 2004. 905

Kutzbach, L., Wille, C., and Pfeiffer, E.-M.: The exchange of carbon dioxide between wet arctic tundra and the atmosphere at the Lena River Delta, Northern Siberia, Biogeosciences, 4, 869–890, doi:10.5194/bg-4-869-2007, 2007. 905

Langer, M., Westermann, S., and Boike, J.: Spatial and temporal variations of summer surface temperatures of wet polygonal tundra in Siberia - implications for MODIS LST based permafrost monitoring, Remote Sens. Environ., 114, 2059–2069, 2010a. 907

Langer, M., Westermann, S., Muster, S., Piel, K., and Boike, J.: Permafrost and surface energy balance of a polygonal tundra site in northern Siberia – Part II: Winter, in preparation, 2010b. 904, 922, 924, 925

Lawrence, D. and Slater, A.: A projection of severe near-surface permafrost degradation during the 21st century, Geophys. Res. Lett., 32, L24401, doi:10.1029/2005GL025080, 2005. 903

Lawrence, D., Slater, A., Romanovsky, V., and Nicolsky, D.: Sensitivity of a model projection of near-surface permafrost degradation to soil column depth and representation of soil organic matter, J. Geophys. Res, 113, F02011, doi:10.1029/2007JF000883, 2008. 903

Lüers, J. and Bareiss, J.: Direct near surface measurements of sensible heat fluxes in the arctic tundra applying eddy-covariance and laser scintillometry – The Arctic Turbulence Experiment 2006 on Svalbard (ARCTEX-2006), submitted to Theor. Appl. Climatol., 2009. 909

Lynch, A., Chapin, F., Hinzman, L., Wu, W., Lilly, E., Vourlitis, G., and Kim, E.: Surface energy balance on the arctic tundra: Measurements and models, J. Climate, 12, 2585–2606, 1999. 923

Mastepanov, M., Sigsgaard, C., Dlugokencky, E., Houweling, S., Ström, L., Tamstorf, M., and Christensen, T.: Large tundra methane burst during onset of freezing, Nature, 456, 628–630, 2008. 903

Mauder, M. and Foken, T.: Documentation and instruction manual of the eddy covariance software package TK2, Univ. of Bayreuth, Dept. of Mikrometeorology, 2004. 908

Mauder, M., Liebethal, C., Göckede, M., Leps, J., Beyrich, F., and Foken, T.: Processing and quality control of flux data during LITFASS-2003, Bound.-Lay. Meteorol., 121, 67–88, 2006. 909

Mauder, M., Foken, T., Clement, R., Elbers, J. A., Eugster, W., Grünwald, T., Heusinkveld, B., and Kolle, O.: Quality control of CarboEurope flux data - Part 2: Inter-comparison of

TCD
4, 901–947, 2010

eddy-covariance software, Biogeosciences, 5, 451–462, doi:10.5194/bg-5-451-2008, 2008. 909
McGuire, A., Chapin, F., Walsh, J., and Wirth, C.: Integrated Regional Changes in Arctic Climate Feedbacks: Implications for the Global Climate System, Ann. Rev. Env. Resour., 31, 61–91, 2006. 903
Nicolsky, D., Romanovsky, V., Alexeev, V., and Lawrence, D.: Improved modeling of permafrost dynamics in a GCM land-surface scheme, Geophys. Res. Lett., 34, L08501, doi:10.1029/2007GL029525, 2007. 903
Nicolsky, D., Romanovsky, V., and Panteleev, G.: Estimation of soil thermal properties using in-situ temperature measurements in the active layer and permafrost, Cold Reg. Sci. Technol., 55, 120–129, 2009. 930
Oke, T.: Boundary layer climates, Methuen, 1987. 910
Overland, J., Wang, M., and Salo, S.: The recent Arctic warm period, Tellus A, 60, 589–597, 2008. 902
Overpeck, J., Hughen, K., Hardy, D., Bradley, R., Case, R., Douglas, M., Finney, B., Gajewski, K., Jacoby, G., Jennings, A., et al.: Arctic environmental change of the last four centuries, Science, 278, 1251, doi:10.1126/science.278.5341.1251, 1997. 902
Peters-Lidard, C., Blackburn, E., Liang, X., and Wood, E.: The effect of soil thermal conductivity parameterization on surface energy fluxes and temperatures, J. Atmos. Sci., 55, 1209–1224, 1998. 924
Pitman, A.: The evolution of, and revolution in, land surface schemes designed for climate models, Int. J. Climatol., 23, 479–510, 2003. 924
Rouse, W., Oswald, C., Binyamin, J., Spence, C., Schertzer, W., Blanken, P., Bussières, N., and Duguay, C.: The role of northern lakes in a regional energy balance, J. Hydrometeorol., 6, 291–305, 2005. 925
Sachs, T., Wille, C., Boike, J., and Kutzbach, L.: Environmental controls on ecosystem-scale CH_4 emission from polygonal tundra in the Lena River Delta, Siberia, J. Geophys. Res.-Biogeo., 113, G00A03, doi:10.1029/2007JG000505, 2008. 903, 905
Schmid, H.: Source areas for scalars and scalar fluxes, Bound.-Lay. Meteorol., 67, 293–318, 1994. 910, 940
Schotanus, P., Nieuwstadt, F., and Bruin, H.: Temperature measurement with a sonic anemometer and its application to heat and moisture fluxes, Bound.-Lay. Meteorol., 26, 81–93, 1983. 908

TCD
4, 901–947, 2010

Serreze, M., Walsh, J., Chapin, F., Osterkamp, T., Dyurgerov, M., Romanovsky, V., Oechel, W., Morison, J., Zhang, T., and Barry, R.: Observational evidence of recent change in the northern high-latitude environment, Climatic Change, 46, 159–207, 2000. 903

Shupe, M. and Intrieri, J.: Cloud radiative forcing of the Arctic surface: The influence of cloud properties, surface albedo, and solar zenith angle, J. Climate, 17, 616–628, 2004. 923

Stendel, M. and Christensen, J.: Impact of global warming on permafrost conditions in a coupled GCM, Geophys. Res. Lett., 29, 1632, doi:10.1029/2001GL014345, 2002. 903

Sturm, M., Holmgren, J., König, M., and Morris, K.: The thermal conductivity of seasonal snow, J. Glaciol., 43, 26–41, 1997. 912

USGS: The Lena River Delta, US Geological Survey: Digital Image, http://eros.usgs.gov/imagegallery/collection.php?type=earth_as_art#26, last access: 8 June 2010, 2000. 940

Viterbo, P., Beljaars, A., Mahfouf, J., and Teixeira, J.: The representation of soil moisture freezing and its impact on the stable boundary layer, Q. J. Roy. Meteor. Soc., 125, 2401–2426, 1999. 924

Westermann, S., Lüers, J., Langer, M., Piel, K., and Boike, J.: The annual surface energy budget of a high-arctic permafrost site on Svalbard, Norway, The Cryosphere, 3, 245–263, doi:10.5194/tc-3-245-2009, 2009. 904, 911, 923, 930

Wilson, K., Goldstein, A., Falge, E., Aubinet, M., Baldocchi, D., Berbigier, P., Bernhofer, C., Ceulemans, R., Dolman, H., Field, C., et al.: Energy balance closure at FLUXNET sites, Agr. Forest Meteorol., 113, 223–243, 2002. 920

Zhang, T.: Influence of the seasonal snow cover on the ground thermal regime: An overview, Rev. Geophys., 43, 1–23, 2005. 912

Zhang, T., Barry, R., Knowles, K., Heginbottom, J., and Brown, J.: Statistics and characteristics of permafrost and ground-ice distribution in the Northern Hemisphere, Polar Geogr., 31, 47–68, 2008.

Zhang, X., Walsh, J., Zhang, J., Bhatt, U., and Ikeda, M.: Climatology and interannual variability of Arctic cyclone activity: 1948–2002, J. Climate, 17, 12, 2300–2317, 2004. 905

Zimov, S., Schuur, E., and Chapin III, F.: Permafrost and the global carbon budget, Science, 312, 1612–1613, 2006. 903

Zhang, T., Barry, R., Knowles, K., Heginbottom, J., and Brown, J.: Statistics and characteristics of permafrost and ground-ice distribution in the Northern Hemisphere, Polar Geogr., 31, 47–68, 2008.

TCD
4, 901–947, 2010

Table 1. Used soil and snow parameters for ground heat flux calculations. Values of porosity P_{dry} and water content θ_w are inferred from soil sample analysis and in situ soil water content measurements. The heat capacities are calculated by weighting $C_{h,w}$ and $C_{h,s}$ according to water content and porosity. The thermal diffusivities D_h are determined with the conductive method (see Sect. 3.3.2), from which we obtain the thermal conductivities K_h in conjunction with the assumed heat capacity. Errors are calculated using Gaussian error propagation.

Substrate	P_{dry}	θ_w	C_h [MJ m^{-3} K^{-1}]	D_h [m^2 s^{-1}]	K_h [W m^{-1} K^{-1}]
dry peat	0.8±0.1	0.1±0.1	0.9±0.5	0.16±0.01	0.14±0.08
wet peat	0.8±0.1	0.7 ±0.1	3.4 ±0.5	0.19±0.04	0.6±0.17
saturated peat	0.8±0.1	0.8±0.1	3.8±0.2	0.19±0.02	0.72±0.08
snow	ρ_{snow}=190±10 kg m^{-3}		0.40±0.04	0.54±0.04	0.22±0.03

TCD
4, 901–947, 2010

Table 2. Average heat fluxes and essential climate parameters. Values are in Wm^{-2}, if not indicated differently. Turbulent heat flux values marked in bold are affected by minor data gaps, due to quality or lee sector data exclusion. Radiation values measured with the NR-Lite sensor are marked with [1], and values obtained with the four component sensor (CNR1) are indicated with [2]. Modeled values of latent heat flux are indicated with [3]. The springtime precipitation is replaced by the snow water equivalent (SWE).

	Spring		Summer		Fall	
	2007 28 Apr–31 May	2008 22 Apr–31 May	2007 12 Jul–23 Aug	2008 7 Jun–8 Jul 29 Jul–30 Aug	2007 1 Sep–30 Sep	2008 1 Sep–30 Sep
Q_{net}	44[1]	27[2]	81[2]	104[2]	7[1]	11[2] 5[1]
ΔQ_S	–	61	119	145	–	–
ΔQ_L	-	-34	–38	–41	–	–
Q_H	**8.7**	**1.3**	14	22	–1.5	–4.4
Q_E	**12**[3]	**9.7**	40	44	**15**[3]	**19**
$Q_{G,\ net}$	18	14	15	20	6	0.5
$Q_{G,\ sensible}$	17	13	5	9	6	4
$Q_{G,\ latent}$	1	1	10	11	0	–3.5
E_{melt} [MJ m^{-2}]	19	19	–	–	–	–
C	**–1.7**	**–3**	12	18	**–12.5**	**–10.1**
T_{surf} [° C]	–3.8	–6.9	10.5	9.2	3	1.2
T_{air} [° C]	–4.7	–6.9	9.2	8.2	2.6	1.6
R_H [%]	84	84	84	84	88	87
P [mm]	SWE: 60	SWE: 57	58	100	49	21

TCD
4, 901–947, 2010

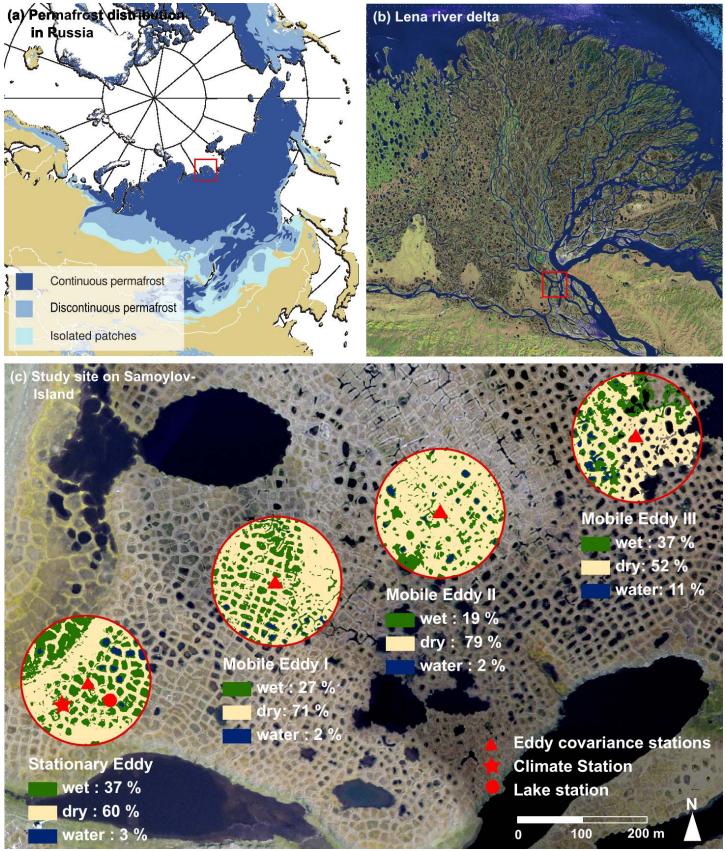

Fig. 1. **(a)** Permafrost distribution in Siberia (Brown et al., 1997); the location of the Lena River delta is marked in red. **(b)** Satellite image of the Lena River delta obtained from the Landsat Thematic Mapper (USGS, 2000); the location of Samoylov Island is marked in red. **(c)** High-resolution aerial image of the study site on Samoylov Island, where the considerable small-scale heterogeneity of the surface cover is visible. The locations of all installations are marked, the approximate footprint areas of the eddy covariance systems are indicated in red. The fractions of wet, dry and water surfaces in the concerning foot print areas are calculated using the foot print model of Schmid (1994).

TCD
4, 901–947, 2010

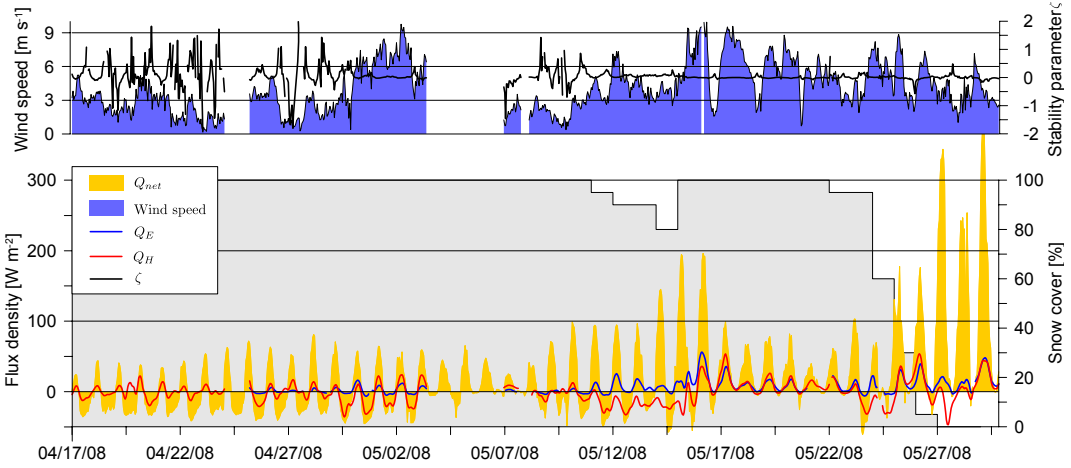

Fig. 2. Net radiation, sensible heat flux, latent heat flux, wind speed, atmospheric stability parameter $\zeta = z/L_*$ and approximate fraction of the snow-covered area (in gray) during spring 2008. The energy balance is strongly related to the evolution of the snow melt. The wind speed is significantly increased during the melt period and the atmospheric stratification is essentially neutral. Varying atmospheric conditions are observed in the pre-melt period.

TCD
4, 901–947, 2010

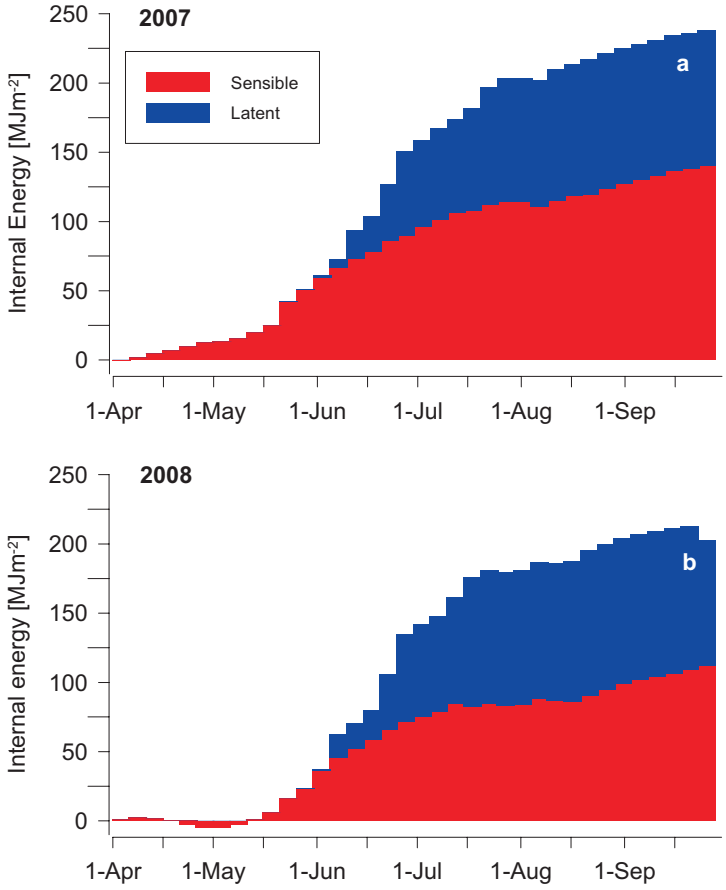

Fig. 3. Internal energy of the soil over the entire observation period in **(a)** 2007 and **(b)** 2008. The soil temperatures of 2007 are colder in spring and the air temperatures are warmer, which explains the increased heat storage at the beginning of the period. Towards the end, the soil temperatures are almost equal.

TCD
4, 901–947, 2010

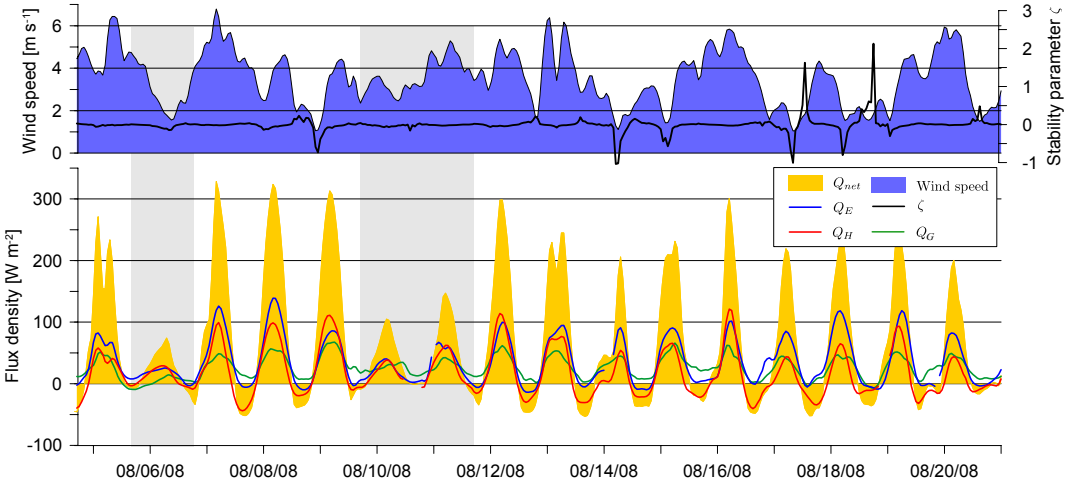

Fig. 4. Exemplary heat fluxes, wind speed and stability parameter during late summer 2008, overcast periods are marked in gray.

TCD
4, 901–947, 2010

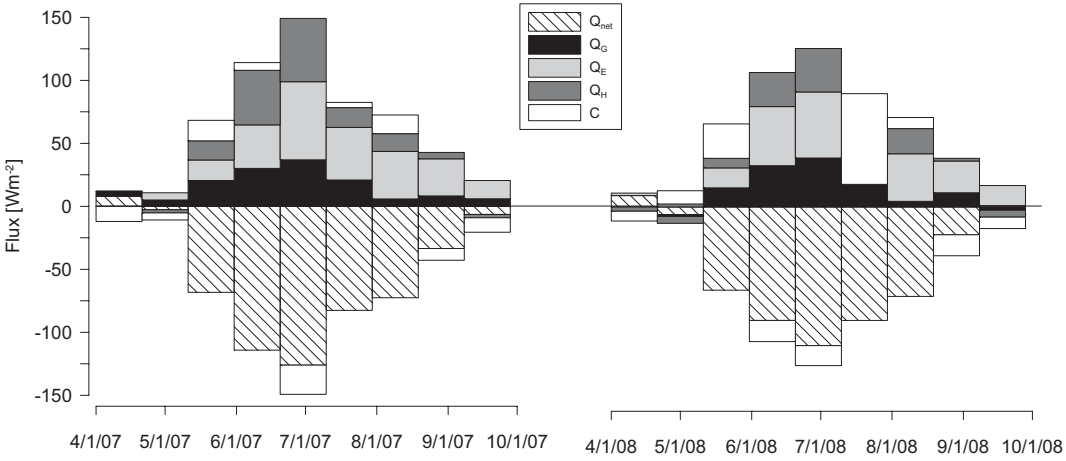

Fig. 5. The energy balance of 2007 and 2008. Heat fluxes are averaged over 20 days and data gaps in the latent heat fluxes are filled by modeled values. Averages are discarded if the data density is less than 60%.

TCD
4, 901–947, 2010

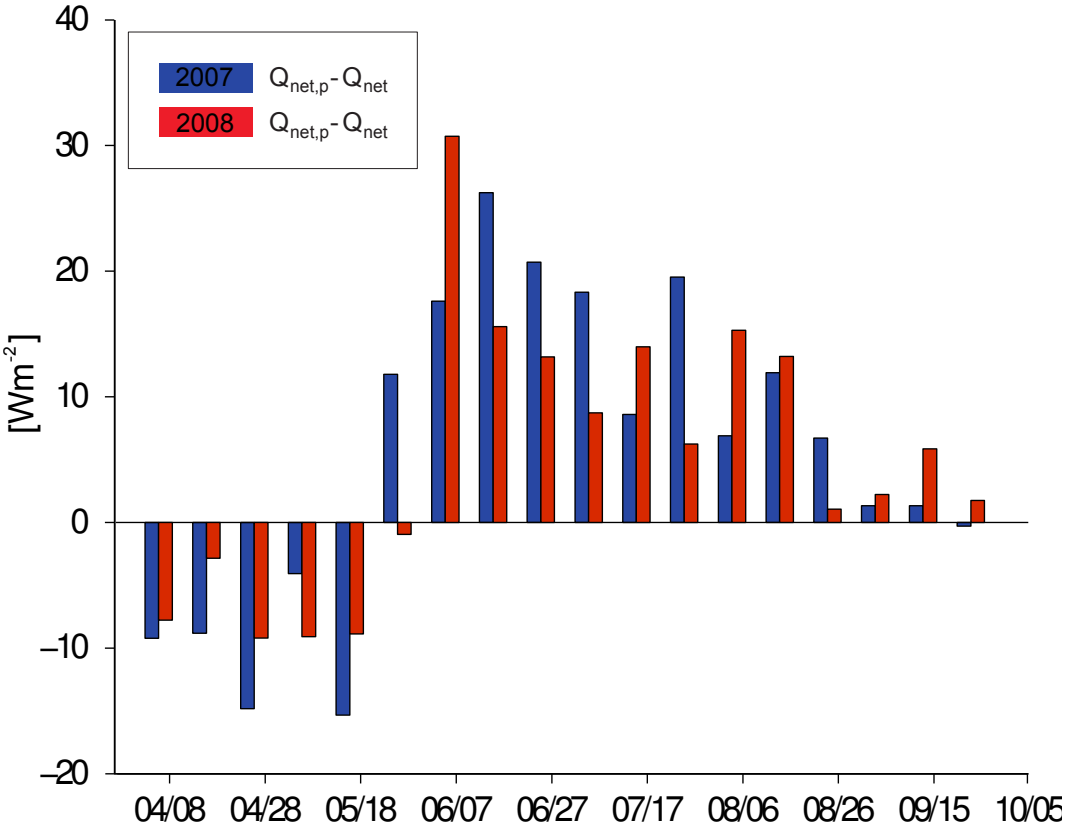

Fig. 6. Differences in the net radiation budget between the pond and the tundra surface during both observation periods in 2007 and 2008.

TCD
4, 901–947, 2010

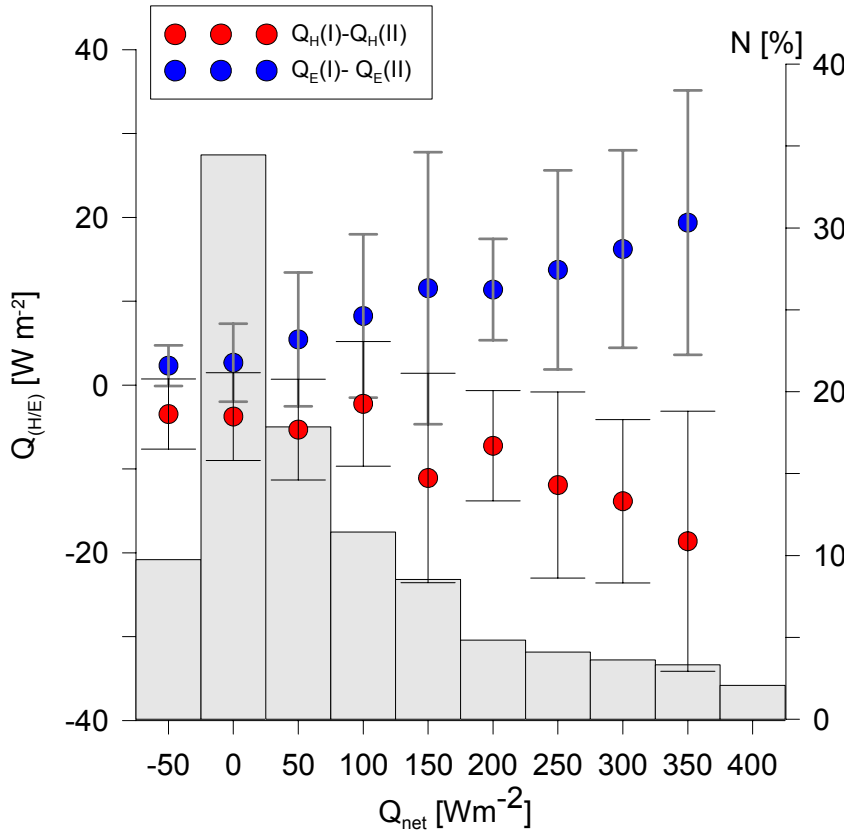

Fig. 7. The differences of the turbulent heat fluxes between the reference station $Q_{H/E}$(I) and the mobile station $Q_{H/E}$(II) at the second location of the mobile eddy system. The flux source area of the second Eddy-Covariance system features a 20% higher fraction of dry surface area. The spatial heat flux differences are directly related to the net radiative forcing. The histogram depicts the distribution of net radiation values during the entire summer period.

TCD
4, 901–947, 2010

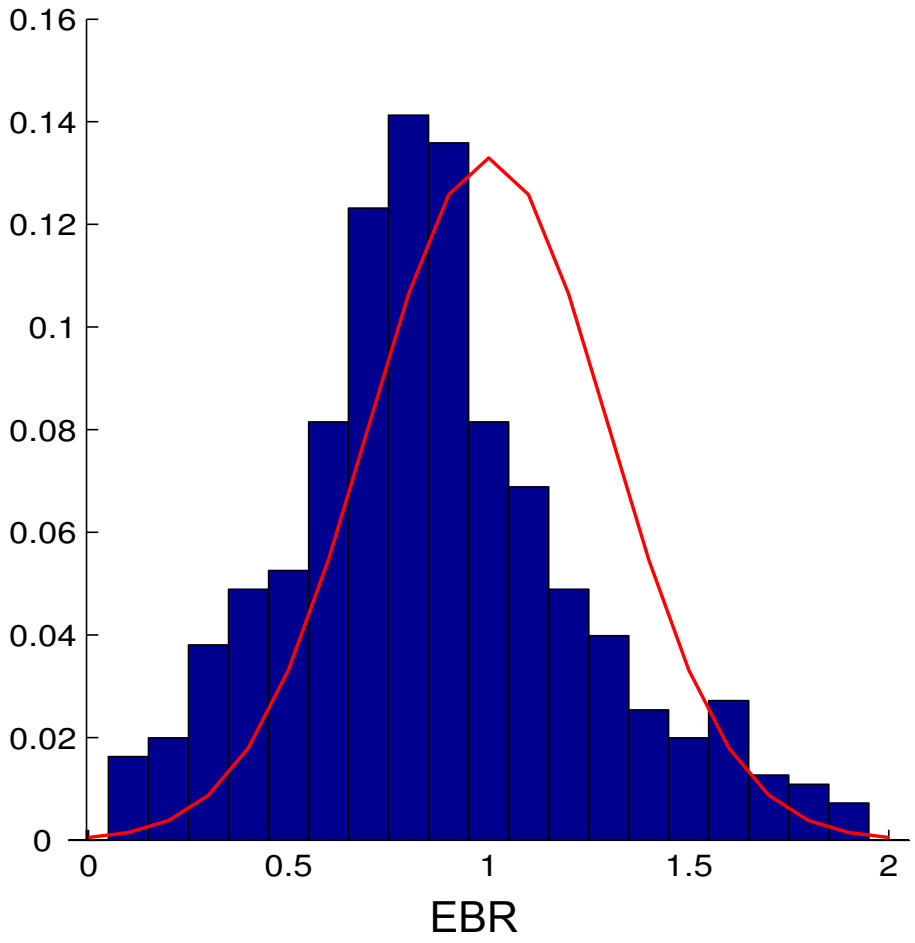

Fig. 8. The Energy balance ration EBR=$(Q_H+Q_E)/(Q_{net}-Q_G)$ measured during the summer period. The red line depicts the normal distribution, which would be expected for a closed surface energy balance with random errors.

TCD
4, 901–947, 2010